Untangling Non-Contact Power Monitoring Puzzles

John S. Donnal, Peter Lindahl, *Member, IEEE*, David Lawrence, Ryan Zachar, and Steven Leeb

***Abstract*— Electromagnetic field sensors provide an electronic "stethoscope" that can determine the current and power flowing in the wire without ohmic contact and without the need to physically separate conductors. Isolation is inherent, and non-contact monitors can be installed without special safety precautions. However, the process of reconstructing the detailed conductor currents is an inverse problem subject to subtle and severe complications in real environments. Interference from nearby conductors, incorrect or unconventional wiring, ground leakage, and three-wire connections complicate the interpretation of electric and magnetic fields to infer line currents. Over a year of field monitoring has been conducted to demonstrate signal processing and physical approaches for untangling these problems to produce accurate and reliable multi-phase power measurements with non-contact sensors.**

***Index Terms*— Digital signal processing, electromagnetic devices, sensor systems and applications.**

I. Introduction

MONITORING and tracking electrical loads with sub-metering for each load is expensive and inconvenient. Sensor networks are difficult to install, expensive to maintain, and leave unaddressed the problem of collating and aggregating data for a complete look at energy scorekeeping [1]. Non-Intrusive Load Monitoring (NILM) provides an exciting alternative. By measuring the electric power at the utility entry point to a building it is possible to identify and track each of the electric loads inside. Significant research has been devoted to load identification and disaggregation [2]–[4]. Unfortunately, all power monitors, traditional or nonintrusive, generally require ohmic contact for voltage measurement and geometric isolation of each phase line for current measurement. The labor costs and downtime associated with this installation deter many potential users.

Non-contact power monitors provide a low cost alternative with no requirement for skilled labor or service interruption. These systems measure per-phase current and voltage by monitoring the electric and magnetic fields outside a power cable with a potentially complex set of phase currents and returns contained in the cable. This approach offers unique opportunities for retrofit monitoring, diagnostic monitoring on high value systems that cannot be shut down, and as a redundant monitor for mission critical systems.

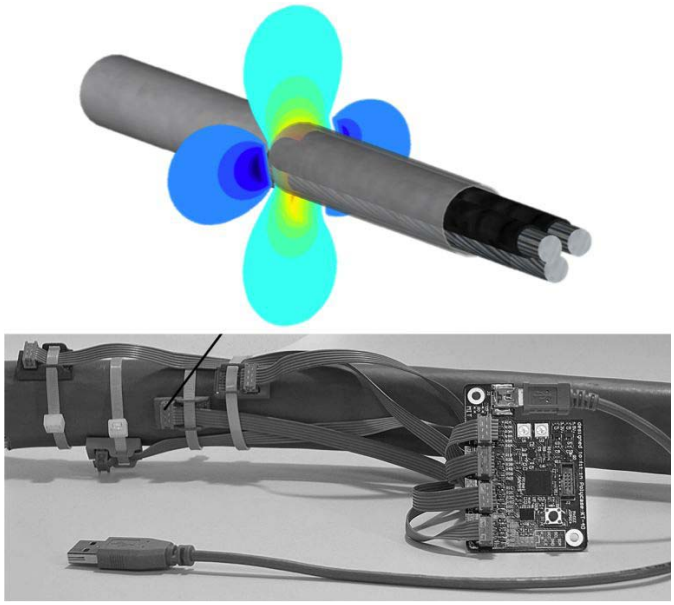

Fig. 1. Although there is zero net flux around a power line, measurements of the magnetic field (shown in the COMSOL visualization at top) can be used to determine the phase currents. The bottom picture shows the non-contact power meter.

Previous work in non-contact power monitoring has focused on sensor design [5]–[8], and calibration with canonical power systems [9]–[11].

This paper presents results from a series of pilot studies conducted to evaluate the performance of these monitors in real world environments including single homes, multi-tenant apartments, and naval ships. The variety of power system configurations and misconfigurations found in the field suggests a revaluation of assumptions implicit in [10]. This work refines and adapts the non-contact calibration and reconstruction algorithms to meet the demands of these different power system puzzles found in real-world environments. These refinements handle all of the interesting pathologies found over the course of the study.

II. Non-Contact Power Monitoring

The non-contact power monitor measures per-phase real and reactive power by sensing the electric and magnetic fields around the surface of a multiphase power line. The system uses multiple magnetic field sensors and a single electric field sensor to perform these measurements. Fig. 1 shows the system installed on a split phase residential power line, and a visualization of the magnetic fields. Each of the four non-contact sensors measures its local magnetic field and attaches to the power line with a cable tie. The sensors are

Manuscript received February 10, 2017; accepted April 11, 2017. Date of publication April 24, 2017; date of current version May 5, 2017. This work was supported in part by the MIT-MASDAR Institute Joint Research Institute, in part by the Office of Naval Research NEPTUNE Program, and in part by The Grainger Foundation. The associate editor coordinating the review of this paper and approving it for publication was Dr. Ferran Reverter. *(Corresponding author: John S. Donnal.)*

J. S. Donnal is with the U.S. Naval Academy in Weapons and Systems Engineering, Annapolis, MD 21402-5000 USA (e-mail: donnal@usna.edu).

P. Lindahl, D. Lawrence, R. Zachar, and S. Leeb are with the Research Laboratory of Electronics, Massachusetts Institute of Technology, Cambridge, MA 02139 USA (e-mail: lindahl@Mit.edu; dlaw@mit.edu; rzachar@mit.edu; sbleeb@mit.edu).

Digital Object Identifier 10.1109/JSEN.2017.2696485

connected by ribbon cable to a control PCB with a SAM4S ARM microcontroller that samples the sensors at 3kHz. This data is sent by USB to a host computer which can be a standard desktop system or an embedded platform like an Intel NUC or Raspberry Pi. The host computer stores the data in a custom time series database optimized for high bandwidth datasets. The data storage and processing architecture are presented in [12] and [13]. A complete discussion of the sensor design and system architecture can be found in [14].

This section presents improved algorithms that can be extended to a wide variety of atypical power systems. These atypical situations have been observed during field studies conducted for this paper in order to test the algorithms presented in [10]. The approach in [10] can be greatly enhanced in robustness and applicability with the improvements presented here. Specifically, four improvements to the sensor hardware and signal processing approach have been found essential for robust field performance. These improvements include: the need to minimize the effect of interfering magnetic fields on the sensing hardware; the ability to automatically detect power system service connections that are different in practice from stated configurations; the ability to detect unplanned current paths such as current carrying earth grounds; and the ability to reliably calibrate three-wire services or similar services that lack a neutral return wire.

A. Reconstruction

We have found that the non-contact calibration and signal reconstruction algorithm described in [10] can fail in some real-world environments. This section briefly reviews the model and algorithm described in [10]. The remaining sections of the paper build on this foundation in order to introduce improved physical sensors and associated signal processing algorithms that are robust in practical situations. Phase vector charts will be used to illustrate key concepts.

Reference [10] introduces a model based on the principle that the magnetic fields generated by currents in a multiphase conductor superimpose linearly. This means that the individual line currents can be reconstructed from measurements of the magnetic field with a suitable linear transform. That is, for each magnetic sensor S_n there is a relationship with phases I_m such that:

$$\begin{aligned} S_1 &= K_{11}I_1 + K_{12}I_2 + \ldots + K_{1M}I_M \\ S_2 &= K_{21}I_1 + K_{22}I_2 + \ldots + K_{2M}I_M \\ &\ldots \\ S_N &= K_{N1}I_1 + K_{N2}I_2 + \ldots + K_{NM}I_M \end{aligned} \tag{1}$$

The system can be inverted if there are at least as many sensors as independent currents and if each of the sensor measurements is linearly independent. For example, the solution for a three phase system with N sensors is

$$\begin{bmatrix} I_A \\ I_B \\ I_C \end{bmatrix} = \begin{bmatrix} K_{11} & K_{12} & K_{13} \\ K_{21} & K_{22} & K_{23} \\ K_{31} & K_{32} & K_{33} \\ & \vdots & \end{bmatrix}^{+} \times \begin{bmatrix} S_1 \\ S_2 \\ S_3 \\ \vdots \end{bmatrix} \tag{2}$$

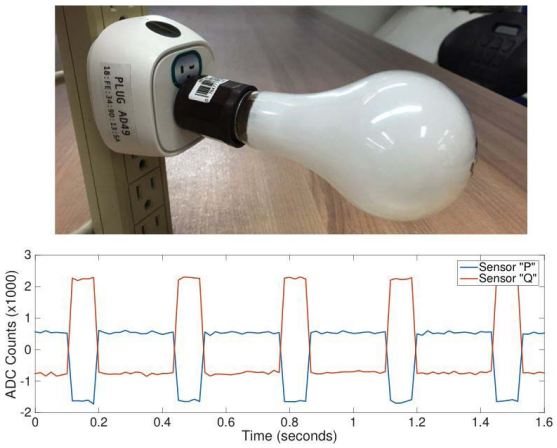

Fig. 2. Top: A microcontroller turns a light bulb on and off repeatedly to generate a power signature used to calibrate non-contact sensors. Bottom: The sensors are sampled by an Analog to Digital Converter (ADC) and separated into P and Q components relative to the measured electric field.

with the constraint that $N \geq 3$. The current flows are then divided into real and reactive components based on their phase relative to the line voltage. The electric field at any point around the power line is linearly proportional to the line voltages with a phase offset that depends on position. Assuming a relatively stiff voltage, as is the case with commercial utilities, a single electric field sensor placed anywhere on the surface of the power line provides enough information to determine the phase of each line voltage.

The voltage phase angles and the transform matrix $[K]$ are determined by a one time calibration procedure performed during the sensor installation.

B. Calibration

A practical non-contact calibration procedure must work on a live power system. Therefore the phase currents are not fixed, or even known during calibration. Instead, a known load is added to the system. The calibration procedure extracts the signature of this known load in isolation from the rest of the power system by a frequency coding scheme.

For example, a known real power load is switched at a fixed frequency and duty cycle. Typically this is an incandescent light bulb like the one shown at the top of Fig. 2. A microcontroller and relay embedded in the plug turn the bulb on and off at the required rate. This produces a periodic modulation in the magnetic field which is detected by the sensors. The calibration waveform is extracted from the utility line frequency using a short-time Fourier Transform producing a plot similar to Fig. 2. The transform is phase aligned to the sensed electric field so that the real content is in phase with the electric field (e-field) sensor and the imaginary content is 90 degrees out of phase. Applying the Fourier Transform again computes the spectral content of the power system transients. In Fig. 2 the calibration load is shown running in isolation. When other loads are operating in the power system, the calibration signature can be extracted from background transients provided that other loads do not switch state at the calibration frequency [10]. Because the load consumes real power, the calibration waveform is in phase with the line voltage. This means the computed ratio of real and imaginary

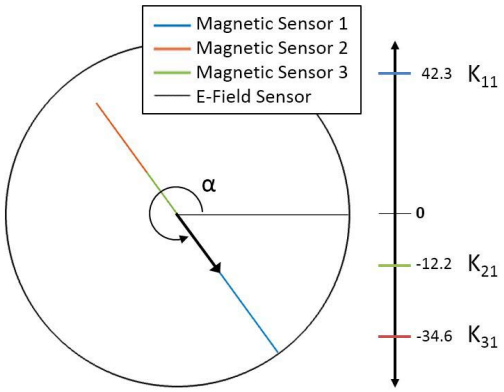

Fig. 3. A Cal sensor responses to a single phase of a power system. The vector magnitudes are coefficients of the transform matrix $[K]$ and the angle α is the phase offset between the line voltage and the e-field sensor.

energy describes the angle between the phase voltage and the electric field as measured by the e-field sensor.

This information can be visualized using the Calibration Vector Chart shown in Fig. 3. The orientation of $\hat{u}$ and the angle α depend on the placement of non-contact sensors around the power line surface. The e-field sensor is shown for reference at zero degrees. Note that all of the magnetic sensor vectors are collinear because they all describe the same calibration event (the same modulated magnetic field) as measured from different points around the power line surface. This one dimensional space is described by the unit vector $\hat{u}$.

$$\alpha = \arctan(\frac{Q_{\text{sensor}}}{P_{\text{sensor}}}) \tag{3}$$

$$\hat{u} = < \cos(\alpha), \sin(\alpha) > \tag{4}$$

This vector points in the direction of real power consumption on the calibrated phase. Any of the sensors can be used to define $\hat{u}$ but in practice using the largest magnitude sensor reduces the numerical error. The sensor coefficients are computed by projecting each sensor vector onto $\hat{u}$ and scaling the result by the calibration load amperage A_{cal}

$$\begin{aligned} K_{11} &= (\vec{S_1} \cdot \hat{u})/A_{cal} \\ K_{21} &= (\vec{S_2} \cdot \hat{u})/A_{cal} \\ &\cdots \\ K_{N1} &= (\vec{S_N} \cdot \hat{u})/A_{cal} \end{aligned} \tag{5}$$

These coefficients form a single column of $[K]$ and are shown in the vertical number line in Fig. 3. Once the calibration load has been placed on all of the phases, the matrix will be complete.

The generalized inverse $[K]^+$ converts magnetic sensor readings into phase currents with Eq.(2). The electric field sensor is then used to convert these into real (P) and reactive (Q) power measurements. The phase of the e-field sensor is used to compute the Fourier Transform of the current. Assuming a stiff utility, the voltage is a constant scale factor (eg $V_{A,B,C} = 120\text{V}_{\text{rms}}$ for US utilities). The product of current and voltage is rotated by the calibration angle α to correct for the offset between the voltage phase and the e-field phase. The complete harmonic power calculations for a three phase system are:

$$\begin{aligned} \vec{P_A} &= V_A \cdot \mathcal{F}\{I_A\} e^{-j\alpha_A} \\ \vec{P_B} &= V_B \cdot \mathcal{F}\{I_B\} e^{-j\alpha_B} \\ \vec{P_C} &= V_C \cdot \mathcal{F}\{I_C\} e^{-j\alpha_C} \end{aligned} \tag{6}$$

Three different sites from our field studies, conducted in several residential and commercial settings and aboard a USCG Cutter, have uncovered four improvements in hardware configuration and signal processing that solve practical problems with applying noncontact sensors in the field. These four improvements are summarized in the following sections. Section III reviews a hardware shielding technique that was found to improve sensor specificity and reduce external interference in residences, commercial facilities, and aboard naval ships. The value of this shielding is illustrated with analytical demonstrations and a laboratory test that reproduces benefits found in our field installations. Section IV presents data from a townhouse in the Boston metropolitan area where split phase power had been unexpectedly replaced with two phases of a three phase power system. A vector chart is introduced to detect this and other voltage angle pathologies, and the approach of [10] can be used once the phase chart is examined. Section V presents power meter data taken in the field at a second residence in the Boston metropolitan area. This data reveals the presence of an unexpected and unmonitored ground return current in the residence. With this knowledge, the noncontact sensor installation is modified to compensate for the additional current path. Experimental verification demonstrates the accurate reconstruction of all currents using noncontact sensors. Finally, Section VI provides a new approach for calibration, extending the methods of [10], to permit the calibration procedure to recognize and train in a multi-phase, no-neutral environment like a 3-wire delta configuration found on-board a USCG Cutter. This new algorithm is demonstrated with field data collected on-board the USCG SPENCER.

III. Improving Sensor Performance: Minimizing Field Interference

During the course of a year long case study, non-contact power monitors were installed in a diverse array of environments including standalone residences, multi-tenant apartments, commercial facilities, and naval ships. In a few of these deployments the calibration and reconstruction algorithm described above failed to produce accurate power measurements. These anomalous installations motivated a deeper analysis of the assumptions in the non-contact algorithm. These assumptions, implied in [10], are listed explicitly below:

1) Fields measured by the sensors are entirely due to currents and voltages inside the power line.
2) KCL holds across the conductors: $\sum I_m = 0$
3) The power system has a neutral bus.

The problematic installations violated one or more of these assumptions. In each case the unmet assumptions can be explicitly compensated for to produce correct power measurements.

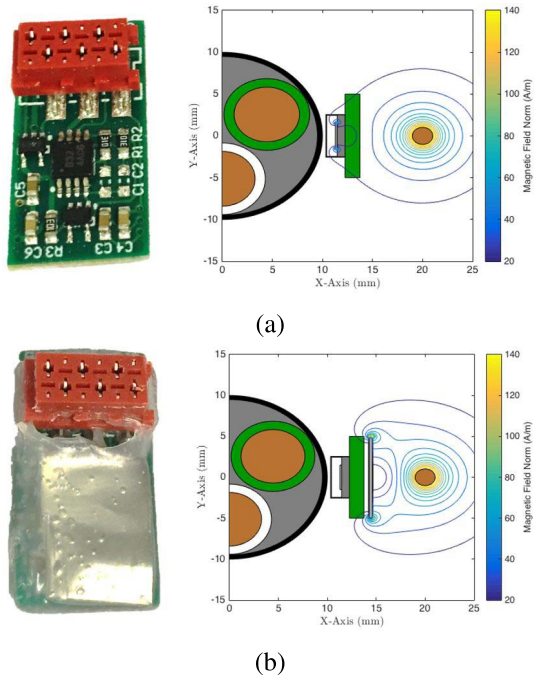

Fig. 4. COMSOL simulations and experimental results show that high permeability shielding on the sensor PCB reduces interference from nearby conductors. (a) Interfering fields from the conductor on the right. (b) Interference reduced with high permeability shielding.

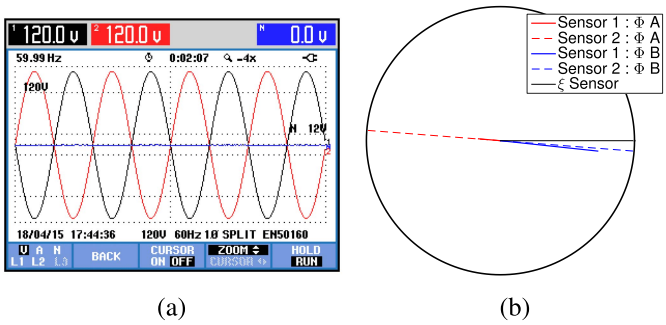

Fig. 5. Non-contact measurements on a split phase power system. The $\hat{u}$ vectors are 180° apart. (a) Fluke measurement. (b) Vector chart.

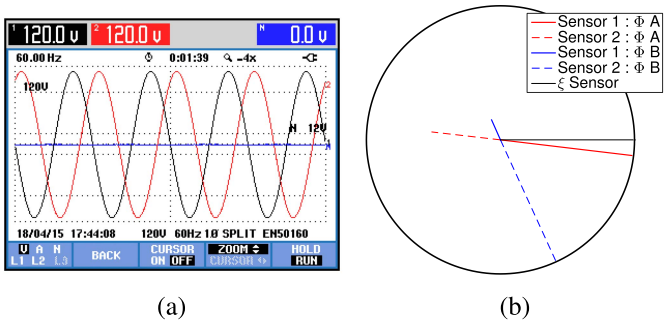

Fig. 6. A residence using two of three phases instead of split phase. This is indicated by $\hat{u}$ vectors 60° or 120° apart. (a) Fluke Measurement. (b) Vector Chart.

Assumption 1 is violated when non-contact sensors pick up fields from conductors other than the power line. This can happen in dense wiring cabinets such as circuit breakers panels. Both the electric and magnetic field sensors are susceptible to interference, but the problem is more acute with magnetic sensors. Even if the electric field sensor picks up nearby voltages this will not interfere with the reconstruction as long as the voltage levels do not change, which is a safe assumption for well regulated utilities. Magnetic fields generated by high currents on nearby wires can result in significant distortion in the reconstruction. Magnetic interference is modeled as an extra term in the rows of Eq.(1) such as:

$$S_1 = K_{11} I_1 + K_{12} I_2 + \epsilon I_m \tag{7}$$

indicating an interfering current I_m on sensor S_1.

For any $|\epsilon| > 0$, I_m will introduce errors in the reconstruction. Fields produced by any I_m must be eliminated, but this is difficult because they do not terminate like electric field lines. Instead, interfering fields must be shunted around the sensor through a high permeability material as illustrated in the COMSOL Multiphysics simulations of Fig. 4. In Fig. 4(a), a sensor intended to monitor the cable bundle on the left (magnetic fields from bundle conductors omitted for clarity), detects a magnetic field emanating from a single stray conductor on the right. This interfering magnetic field however can be shunted through a mu-metal [15] shield attached to the opposite side of the sensor PCB as shown in the Fig. 4(b).

Laboratory tests of mu-metal shields confirm these COMSOL simulations and reveal an important trade off when considering shielding design. Increasing the surface area of the shield improves the sensors immunity to stray fields, but it also decreases the pickup's overall sensitivity. In practice the improvement in sensor specificity more than compensates for the decrease in sensitivity. Lab tests with the shielding geometry in Fig. 4(b) show a gain reduction of -1dB for a 5dB improvement in signal rejection ratio. For even more interference attenuation, the sensor and wire bundle can be wrapped with shielding material which reduces gain by -2.5dB for a 14.5dB improvement in signal rejection ratio.

IV. Detecting Power System Abnormalities

During the pilot study seven non-contact systems were deployed in residences across the Boston and Cambridge metropolitan area. Even with the relatively small sample size, the study revealed an unexpected diversity of installed power systems.

Traditional residential power systems are split phase. A split phase system is built by center tapping a transformer for neutral and delivering the two legs as *Phase A* and *Phase B*. The legs are 180 degrees out of phase which provides doubled voltage for high energy appliances like clothes dryers. Fig. 5(a)shows the voltage waveforms in a split phase power system as measured by a Fluke power meter. Fig.5(b) shows a Calibration Vector Chart for sensors installed on this power system. The α angles are offset from 0° and 180° due to the frequency response of the electric field sensor. The sensor has a hardware integration circuit with a 3° offset at 60 Hz [10].

Any split phase system should have a similar Calibration Vector Chart. However, a non−contact system in an older Boston town house produced the chart shown in Fig. 6(b).

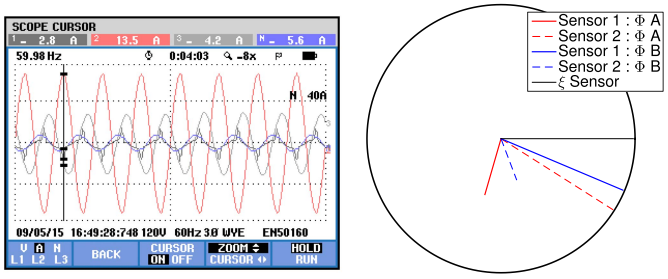

(a) (b)

Fig. 7. A residence with ground leakage. The sensor phase responses are not collinear indicating an alternate current path in the power system. (a) Fluke Measurement. (b) Vector Chart.

The angle between the $\hat{u}$ vectors is 60°. This response could be produced by voltage phases that are either 60° or 120° apart. The ambiguity is a result of $\hat{u}$ being determined by the strongest magnetic sensor response. This response is either dominated by fields from the neutral wire or the phase wire. If $\hat{u}$ is aligned with the neutral wire it will have an apparent −180° offset from the true phase voltage. In this case the sensor is likely aligned with neutral which indicates that the building has two of three phases rather than split phase. This was confirmed with a Fluke power meter installed in the dryer outlet showing the voltage waveforms in Fig. 6(a). The calibration process is agnostic to the voltage configuration so the reconstruction algorithm still returns the correct power information despite the atypical Calibration Vector Chart. This case illustrates the chart's utility in determining the phase configuration. This can be particularly useful when contact meters like the Fluke are cost prohibitive or there is no access to a multiphase outlet.

V. Detecting Ground Current Return

Wiring a building with two of three phases is atypical but does not present safety concerns. Another residence had a much more serious configuration error. Experimental data collected at the site documenting this error is shown in Fig. 7(a). The experimental data from the non-contact sensors in this multi-tenant residence in Cambridge has been used to create the phase vector chart shown in Fig. 7(b).

These experimentally observed phase sensor responses are not collinear. This indicates multiple return paths for a phase current and further that these paths have different impedances. This invalidates Assumption 2: that KCL must hold across the power line conductors. Investigation with a Fluke power meter confirmed positive net flux around the power line indicating a positive net current into the building. The alternate return path was through the building's water pipe which serves as the grounding point. All four current branches were measured by a Fluke current meter shown in Fig. 8. The meter is designed to measure a three phase power system so the *Phase C* sensor was repurposed to measure the ground wire. The measurements in Fig. 7a show a non-zero ground current equal to the sum of the neutral and phase currents. The exact cause of the ground leakage is not known and difficult to

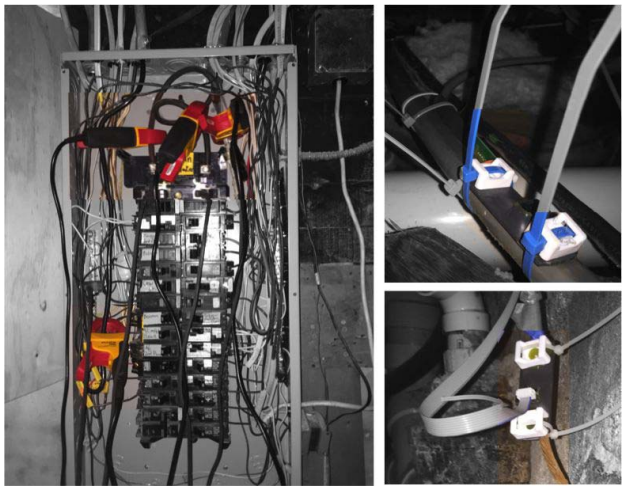

Fig. 8. Detecting ground leakage in a power system (left). Non-contact sensors installed on power line and ground wire (right).

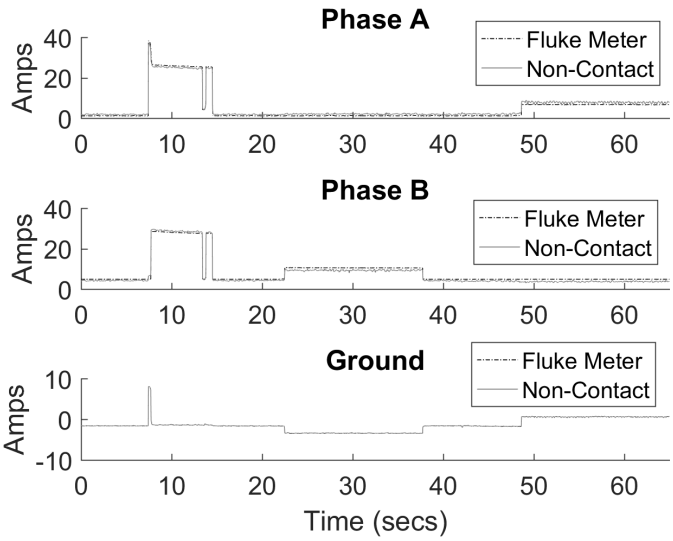

Fig. 9. Non-contact sensors can reconstruct ground leakage when calibrated by multidimensional regression.

diagnose without shutting off power to the block. It is likely due to the combination of a low impedance path through the water pipe and inductance on the neutral line. This inductance could come from various sources such as a coil of extra neutral wire stored in the pole transformer.

Due to the multiple current paths, this system cannot be calibrated using the algorithm presented in Section II-B. However, the system is still linear and placing an extra sensor on the ground wire provides a measurement space that can be inverted into phase currents. The right hand side of Fig. 8 shows the non-contact sensor configuration. Two sensors are placed on the power line (top) and an extra sensor is attached to the bond wire on the water pipe (bottom).

The system is calibrated by correlating time domain Fluke current sensor measurements with the non-contact sensor measurements. A least-squares $[K]$ matrix can be found using multidimensional regression. With Eq. (2) this matrix can be used to reconstruct the phase and ground leakage currents from the non-contact sensors. Fig. 9 shows both phases and the

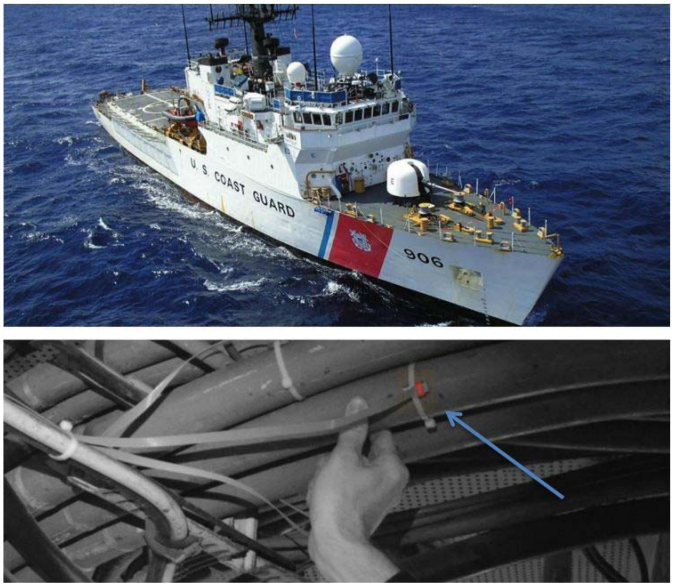

Fig. 10. USCGC Spencer instrumented with non-contact sensors. Marine power systems can be monitored with non-contact sensors but the insulated neutral topology requires a more complex calibration procedure.

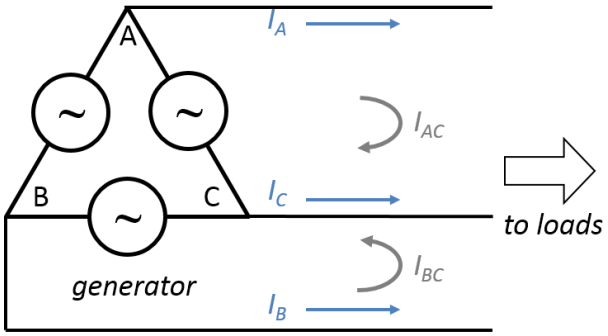

Fig. 11. An insulated neutral power system. All loads draw l system to two independent current loops (I_{AC}, I_{BC}). The non-contact sensors infer branch currents I_A, I_B, and I_C from calibration across I_{AC} and I_{BC}.

ground current as measured by both the non-contact sensors and the Fluke current meter.

VI. Calibrating Without a Neutral Connection

On a ship certain equipment must remain operational to ensure the safety of the crew. Therefore, uninterrupted power delivery is a top priority. Most marine power systems such as the Coast Guard Cutter shown in Fig. 10 use an insulated neutral configuration (Fig. 11) to improve the ship's resilience to electrical grounding faults [16]. A ground fault occurs when a phase line contacts the equipment chassis. If the ship used a traditional earthed neutral this would result in a large current flow through the hull and back to the generator. This current flow could damage the generator and trip current limit devices bringing critical equipment offline. A ground fault in an insulated neutral system will not cause a short circuit and equipment will continue to operate normally. A power failure only occurs when two separate phases both suffer a ground fault simultaneously.

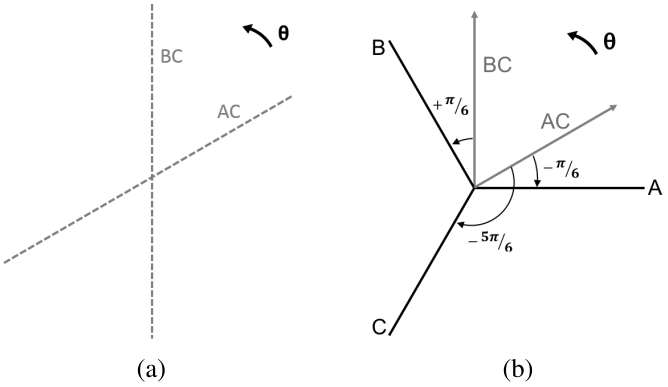

Fig. 12. Line-line calibration vectors provide sufficient information to reconstruct an insulated neutral system. (a) Line-line calibration. (b) Expected relationship.

Instrumenting an insulated neutral power system with non-contact sensors requires a more complex calibration procedure. The lack of a neutral bus violates Assumption 3 and means that the phases cannot be excited individually. This reduces the system to two independent currents as shown in Fig. 11. While the system is functionally two line-line phases, it is traditionally measured as three line-neutral phases for compatibility with its earthed neutral counterpart. The calibration process is adapted to transform the two independent line-line phases in Fig. 12(a) into the three dependent line-neutral phases in Fig. 12(b).

The process begins by connecting a calibration load to two different pairs of line-line phases generating a $N \times 2$ line-line calibration matrix $[K_{LL}]$ using the algorithm presented in Section II -B. This matrix converts sensor measurements into line-line currents. Just as the case with the wall outlet calibrator in Fig. 2, the particular line-line pair that is calibrated first is not important and in practice is often not known. On a three phase non-contact power monitor, the phase names are unknown but the phase order is fixed. The voltage waveform zero crossings are ordered in time ($A \rightarrow B \rightarrow C$) which is indicated by θ in Fig 12. Given an unlabeled three phase outlet, assigning a phase label to a single wire unambiguously labels the phase of the other two wires as well. By convention the calibration procedure labels the phase common to both calibration events as *Phase C*, making it analogous to the neutral in a two phase system. The line-neutral phases shown in Fig. 11 are reconstructed by KCL as

$$\begin{aligned} I_A &= I_{AC} \\ I_B &= I_{BC} \\ I_C &= -(I_{AC} + I_{BC}) \end{aligned} \tag{8}$$

The $N \times 2$ line-line calibration matrix $[K_{LL}]$ is inverted as in the grounded neutral case and the conversion from line-line currents to line-neutral currents is done by the 3×2 compensation matrix $[P]$

$$\begin{bmatrix} I_A \\ I_B \\ I_C \end{bmatrix} = [P][K_{LL}]^{+} \begin{bmatrix} S_1 \\ \vdots \\ S_N \end{bmatrix} \tag{9}$$

The structure of $[P]$ and the voltage phase angles are determined during calibration as explained below.

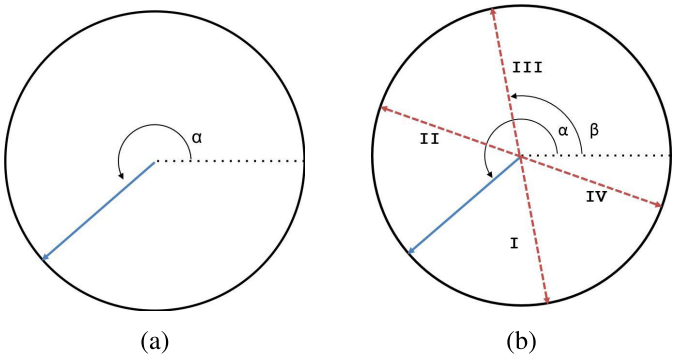

Fig. 13. Non-contact Vector Chart for insulated neutral calibration. Four possible $\hat{u}$, $\hat{u}$) combinations depending on sensor placement and calibration order. (a) First line-line calibration produces $\hat{u}$ with offset α. (b) Second line-line calibration produces $\hat{u}$ with offset β.

Fig. 13(a) shows a possible Calibration Vector Chart after calibration on a single line-line pair. The angle α indicates the phase offset between the electric field sensor and the line-line voltage used for this calibration. Calibration on a second line-line pair produces one of four possible $\hat{u}$ vectors indicated by dashed arrows in Fig. 13(b). The four cases are the result of (1) the order of calibration and (2) ambiguity in the orientation of $\hat{u}$.

The relationship between α and β determines the calibration scenario and the alignment of the phase voltage vectors. The detection and compensation for each of these four scenarios is described in the following sections.

A. Detecting Calibration Order

The voltage phases rotate counter-clockwise as indicated by θ in Fig. 12. Therefore the phase difference between line-line voltage BC and line-line voltage AC is positive 60 degrees. Case I is a result of placing the calibration load across AC first, and then BC producing $\hat{u}$ vectors which also rotate counter-clockwise as shown in Fig. 14(a). In this case α and β are in phase order:

$$\begin{aligned} \alpha &= \angle\vec{AC} + \angle\vec{E}_{\text{sensor}} \\ \beta &= \angle\vec{BC} + \angle\vec{E}_{\text{sensor}} \\ \text{Case I}(\beta - \alpha) &= \angle\vec{BC} - \angle\vec{AC} = 60^\circ \end{aligned} \tag{10}$$

so the compensation matrix in Eq.(9) is:

$$[P] = \begin{bmatrix} 1 & 0 \\ 0 & 1 \\ -1 & -1 \end{bmatrix} \tag{11}$$

and the phase angles for Eq.(6) follow geometrically from Fig. 12(b):

$$\begin{aligned} \alpha_A &= \alpha - \pi/6 \\ \alpha_B &= \beta + \pi/6 \\ \alpha_C &= \alpha - 5\pi/6 \end{aligned} \tag{12}$$

In Case II the calibration order is reversed. Here the first $\hat{u}$ is aligned with $\vec{BC}$ and the second $\hat{u}$ is aligned with $\vec{AC}$ which results in the angular difference:

$$\text{Case II}(\beta - \alpha) = \angle\vec{AC} - \angle\vec{BC} = -60^\circ \tag{13}$$

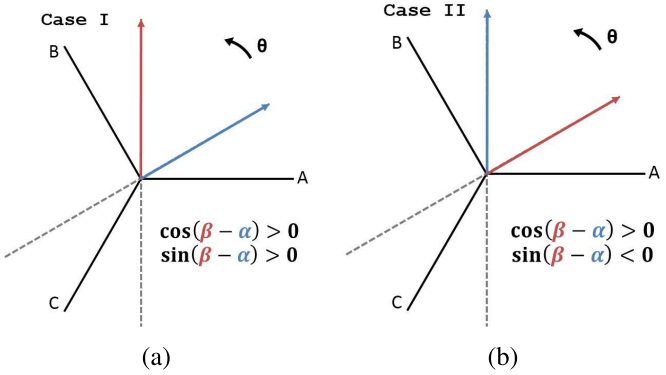

Fig. 14. Calibration with ± 60° angular difference. (a) Case I. (b) Case II * FIX.

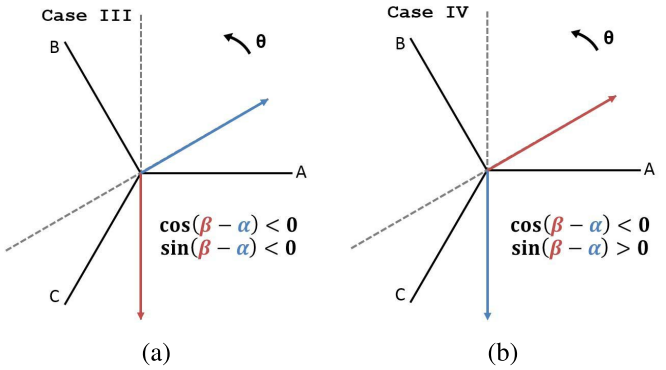

Fig. 15. Calibration with ±120° angular difference. (a) Case III. (b) Case IV.

In this case the columns of $[P]$ are swapped in Eq.(11) and α and β are exchanged in Eq.(12).

B. Detecting $\hat{u}$ Orientation

There is a fundamental ambiguity in the sign of $\hat{u}$ as discussed in Section IV. This ambiguity is partially resolved by convention by assuming that the $\hat{u}$ associated with *Phase A* points along $\vec{AC}$. That is, for one of the $\hat{u}$ vectors:

$$\hat{u} \cdot \vec{AC} > 0 \tag{14}$$

The direction of the $\hat{u}$ vector associated with *Phase B* must be determined analytically (either $\vec{BC}$ or $\vec{CB}$). In Cases I and II the sensor with the strongest sensitivity to I_{BC} is physically closer to the *Phase B* wire so the $\hat{u}$ vector points along $\vec{BC}$. If this sensor is instead closer to the *Phase C* wire or physically flipped 180° then $\hat{u}$ will point along $\vec{CB}$. Cases III and IV in Fig. 15 illustrate this scenario. The angular differences in these cases are:

$$\begin{aligned} \text{Case III}(\beta - \alpha) &= \angle\vec{CB} - \angle\vec{AC} = -120^\circ \\ \text{Case IV}(\beta - \alpha) &= \angle\vec{AC} - \angle\vec{CB} = 120^\circ \end{aligned} \tag{15}$$

In Case III, the $\hat{u}$ vector is flipped back to the $\vec{BC}$ direction with the compensation matrix:

$$[P] = \begin{bmatrix} 1 & 0 \\ 0 & -1 \\ -1 & 1 \end{bmatrix} \tag{16}$$

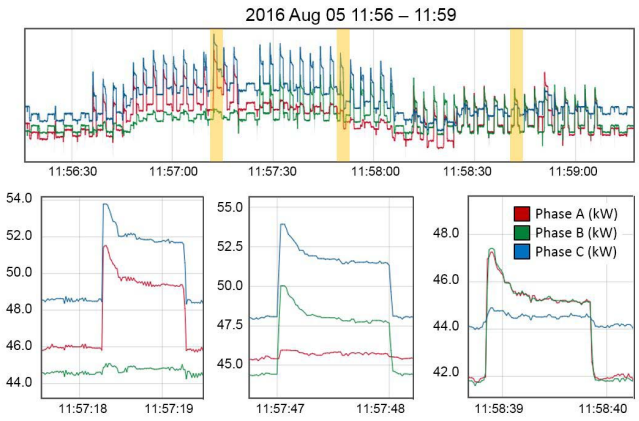

Fig. 16. Total power consumption of the USCGC Spencer as measured by non-contact sensors. The subfigures highlight the calibrator waveform as it is connected to across each line-line pair.

TABLE I
POSSIBLE CALIBRATION SCENARIOS

		$\sin(\beta-\alpha)$	
		+	-
$\cos(\beta-\alpha)$	+	Case I	Case II
	-	Case IV	Case III

and the phase angles become:

$$\begin{aligned} \angle A &= \alpha - \pi/6 \\ \angle B &= \beta + \pi/6 + \pi \\ \angle C &= \alpha - 5\pi/6 \end{aligned} \tag{17}$$

In Case IV the order of calibration is flipped as well so the columns of $[P]$ in Eq.(16) are exchanged and α and β are exchanged in Eq.(17).

C. Determining the Calibration Scenario

There are four possible angular differences $[\pm 60, \pm 120]$ each corresponding to one of the calibration scenarios described. These angles fall in different quadrants so the calibration case can be determined by the sine and cosine of the angular difference. Table I shows the relationships between calibration scenario and angular differences. These relationships are also highlighted in Figs. 14 and 15. This determinant is efficient to compute and numerically robust.

D. USCGC Spencer Case Study

The USCGC Spencer in Fig. 10 is a 270 WEMAC class cutter. Non-contact sensors were installed on the main phase lines with plastic cable ties. The calibration was performed with a relay controlled 8kW resistive heater run alternately on two different line-line pairs. After running the calibration algorithm, the heater was run on all three line-line pairs to verify the correct phase disaggregation. Fig. 16 shows the heater running on each line-line pair and switching at the calibration frequency. The ship was operational throughout the calibration process so the heater waveform is superimposed on top of the ship's baseline electric load. Further details of this particular study are presented in [17]

VII. CONCLUSION

Non-contact power monitors can be installed without skilled labor and without any interruption in service. These monitors potentially open exciting new markets in load monitoring and power system diagnostics. This paper introduces new algorithms for gracefully and accurately handling operational environments with diverse physical and electrical configurations and misconfigurations. By explicitly compensating for assumptions implied in [10], non-contact sensors can be adapted to accurately monitor a wide variety of power systems. These sensors and algorithms have been proven over the course a year long study in diverse residential, commercial, and maritime environments used to provided the examples reviewed in this paper.

REFERENCES

[1] K. Dorling, G. G. Messier, S. Valentin, and S. Magierowski, "Minimizing the net present cost of deploying and operating wireless sensor networks," *IEEE Trans. Netw. Service Manage.*, vol. 12, no. 3, pp. 511–525, Sep. 2015.
[2] H. H. Chang, M. C. Lee, W. J. Lee, C. L. Chien, and N. Chen, "Feature extraction-based hellinger distance algorithm for nonintrusive aging load identification in residential buildings," *IEEE Trans. Ind. Appl.*, vol. 52, no. 3, pp. 2031–2039, May 2016.
[3] D. Egarter, V. P. Bhuvana, and W. Elmenreich, "PALDi: Online load disaggregation via particle filtering," *IEEE Trans. Instrum. Meas.*, vol. 64, no. 2, pp. 467–477, Feb. 2015.
[4] J. M. Gillis, S. M. Alshareef, and W. G. Morsi, "Nonintrusive load monitoring using wavelet design and machine learning," *IEEE Trans. Smart Grid*, vol. 7, no. 1, pp. 320–328, Jan. 2016.
[5] D. Lawrence, J. S. Donnal, S. Leeb, and Y. He, "Non-contact measurement of line voltage," *IEEE Sensors J.*, vol. 16, no. 24, pp. 8990–8997, Dec. 2016.
[6] D. Balsamo, D. Porcarelli, L. Benini, and B. Davide, "A new non-invasive voltage measurement method for wireless analysis of electrical parameters and power quality," in *Proc. IEEE Sensors*, Nov. 2013, pp. 1–4.
[7] K. M. Tsang and W. L. Chan, "Dual capacitive sensors for non-contact ac voltage measurement," *Sens. Actuators A, Phys.*, vol. 167, pp. 261–266, Jun. 2011.
[8] J. S. Bobowski, M. S. Ferdous, and T. Johnson, "Calibrated single-contact voltage sensor for high-voltage monitoring applications," *IEEE Trans. Instrum. Meas.*, vol. 64, no. 4, pp. 923–934, Apr. 2015.
[9] X. Sun, Q. Huang, Y. Hou, L. Jiang, and P. W. T. Pong, "Noncontact operation-state monitoring technology based on magnetic-field sensing for overhead high-voltage transmission lines," *IEEE Trans. Power Del.*, vol. 28, no. 4, pp. 2145–2153, Oct. 2013.
[10] J. S. Donnal and S. B. Leeb, "Noncontact power meter," *IEEE Sensors J.*, vol. 15, no. 2, pp. 1161–1169, Feb. 2015.
[11] D. Lawrence, J. S. Donnal, and S. Leeb, "Current and voltage reconstruction from non-contact field measurements," *IEEE Sensors J.*, vol. 16, no. 15, pp. 6095–6103, Aug. 2016.
[12] J. Paris, J. S. Donnal, and S. B. Leeb, "NilmDB: The non-intrusive load monitor database," *IEEE Trans. Smart Grids*, vol. 5, no. 5, pp. 2459–2467, Sep. 2014.
[13] J. S. Donnal, J. Paris, and S. B. Leeb, "Energy applications for an energy box," in *IEEE Internet Things J.*, vol. 3, no. 5, pp. 787–795, Oct. 2016, doi: 10.1109/JIOT.2016.2560123.
[14] J. Donnal, "Wattsworth: A vision for cyber physical system design," Ph.D. dissertation, Dept. Elect. Eng. Comput. Sci., Massachusetts Inst. Technol., Cambridge, MA, USA, Jun. 2016.
[15] *High Permeability ASTM A753 Alloy Type 4*, MuShield Company, Londonderry, NH, USA, Aug. 2016.
[16] M. R. Patel, *Shipboard Electrical Power Systems*. Boca Raton, FL, USA: CRC Press, Dec. 2011.
[17] P. Lindahl, S. Leeb, J. Donnal, and G. Bredariol, "Noncontact sensors and nonintrusive load monitoring (NILM) aboard the USCGC Spencer," in *Proc. IEEE AUTOTESTCON*, Sep. 2016, pp. 1–10.

John S. Donnal received the B.S. degree from Princeton University, Princeton, in 2007, and the M.S. and Ph.D. degrees from the Massachusetts Institute of Technology, in 2013 and 2016, respectively, all in electrical engineering. His research interests include nonintrusive load monitoring synthesis, energy harvesting, and communications systems. He is currently a Faculty Member of the U.S. Naval Academy in Weapons and Systems Engineering.

Peter Lindahl (S'08–M'15) received the Ph.D. degree in engineering from Montana State University, Bozeman, MT, USA, in 2013. He is currently a Post-Doctoral Associate with the Research Laboratory of Electronics, Massachusetts Institute of Technology, Cambridge, MA, USA. His current research interests include nonintrusive sensing and instrumentation, smart-building technologies, energy efficiency, renewable energy generation, and energy policy.

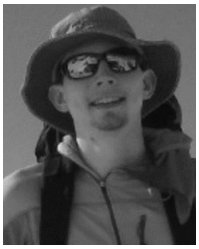

David Lawrence received the M.Eng. degree from the Massachusetts Institute of Technology in 2016. He is currently with MarkForged, Cambridge, MA, USA.

Ryan Zachar received the Graduate degrees from the Department of Mechanical Engineering, MIT, while working in the Electromechanical Systems Group. He is currently a U.S. Navy officer. He received the Naval Sea Systems Command Award for Naval Construction and Engineering for his thesis work on new techniques for vibration monitoring in USN vessels.

Steven Leeb received the Ph.D. degree from the Massachusetts Institute of Technology in 1993. He has been a Faculty Member with the Department of Electrical Engineering and Computer Science, MIT, since 1993. He also holds a joint appointment with the Department of Mechanical Engineering, MIT. He is concerned with the development of signal processing algorithms for energy and real-time control applications.